PAPER • **OPEN ACCESS**

Dual absorber Fe_2O_3/WO_3 host-guest architectures for improved charge generation and transfer in photoelectrochemical applications

To cite this article: Alexander Müller *et al* 2017 *Mater. Res. Express* **4** 016409

Materials Research Express

OPEN ACCESS

RECEIVED
29 November 2016

REVISED
13 December 2016

ACCEPTED FOR PUBLICATION
5 January 2017

PUBLISHED
30 January 2017

PAPER

Dual absorber Fe_2O_3/WO_3 host-guest architectures for improved charge generation and transfer in photoelectrochemical applications

Alexander Müller[1,2,3,4], **Ilina Kondofersky**[2,4], **Alena Folger**[1], **Dina Fattakhova-Rohlfing**[2], **Thomas Bein**[2] and **Christina Scheu**[1]

[1] Max-Planck-Institut für Eisenforschung GmbH (MPIE), Max-Planck-Strasse 1, 40237 Düsseldorf, Germany
[2] Department of Chemistry and Center for NanoScience (CeNS), University of Munich (LMU), Butenandtstrasse 5-13, 81377 Munich, Germany
[3] Present address: National Center for Electron Microscopy, Molecular Foundry, Lawrence Berkeley National Laboratory, 1 Cyclotron Rd, Berkeley, CA 94720, United States of America
[4] These authors contributed equally.

E-mail: scheu@mpie.de

Keywords: photoelectrochemical water splitting, WO_3, Fe_2O_3, dual absorber, oxide heterostructure, photoanodes, host-guest architecture

Supplementary material for this article is available online

Abstract

In this study the influence of the spatial distribution and of different nanostructures of WO_3 and Fe_2O_3 in the dual absorber system Fe_2O_3/WO_3 was systematically investigated for the first time. WO_3 was applied as a scaffold and/or as a surface treatment to mesoporous Fe_2O_3 films. Both approaches strongly increased the performance compared to the individual photoabsorbers. By combining a host guest architecture with a surface treatment, current densities of about 0.7 mA cm^{-2} at 1.23 V versus reversible hydrogen electrode under AM 1.5 illumination with an incident photon-to-current efficiency of 17% at 350 nm were achieved without the use of further catalysts. We could identify several beneficial interactions between Fe_2O_3 and WO_3. WO_3 strongly scatters visible light, resulting in increased absorption by Fe_2O_3 and higher current densities. We also determined a cathodic shift in the onset potential to 0.8 V and increased transfer rates of up to 88%. This combination of beneficial effects proves the viability of the presented device architecture.

1. Introduction

Driven by climate change, rapid population growth and dwindling resources, research into alternative, sustainable energies is thriving. Solar cells and wind turbines, which harness the power of the sun, already play a major role in the energy mix of some countries, with their market share expected to increase. However, storage of the generated electricity is a challenge. One of many possible solutions is photoelectrochemical water splitting, which uses sun light as an energy source to generate oxygen and hydrogen from water. While suitable photoelectrode materials have been studied since 1972 [1], research has intensified in the last few years and several photocathode and photoanode materials (such as TiO_2, Si or Cu_2O and Fe_2O_3, WO_3 or $BiVO_4$, respectively) have been investigated [2–4]. Efficient photoanodes, in particular, are difficult to realize. Producing one oxygen molecule requires four holes, making recombination likely and requiring significant optimization of factors such as composition, electronic structure and morphology. All efforts notwithstanding, it is becoming more and more obvious that limitations intrinsic to many single absorber materials investigated so far, such as large band gaps, slow surface kinetics or fast bulk electron–hole recombination, are difficult to overcome. One approach towards solving this problem is the combination of different photoabsorber materials. Such a combination can increase the efficiency in several ways such as by optical absorption enhancement, enhanced charge separation, faster surface kinetics, or the modification of the electronic structure of the interface between both materials [5]. For photoanodes, a dual absorber approach has been successful for several systems such as WO_3/TiO_2 [6], $WO_3/BiVO_4$ [7], TiO_2/Fe_2O_3 [8] and Fe_2O_3/WO_3 [5, 9, 10].

The Fe_2O_3/WO_3 system is a good model and a promising photoanode for many reasons. The individual materials are abundant and therefore cheap, non-toxic and corrosion-resistant [11, 12]. Consequently, both materials have been intensively studied, and the influence of different morphologies, dopants, surface modifications etc for both systems is well-investigated [11, 13]. WO_3 has a band gap of 2.5–2.8 eV and absorbs mostly in the blue and UV spectral range [12, 14, 15]. Because of good charge transport properties and fast surface kinetics, it has proven itself a suitable candidate for water photoelectrolysis [15]. However, the large band gap limits the overall theoretical solar-to-hydrogen efficiency to 8% [16]. Fe_2O_3, on the other hand, has a band gap between 1.9 and 2.2 eV and also absorbs a large fraction of visible light, driving the potential solar-to-hydrogen efficiency up to 16.8% [11, 16]. Unfortunately, the expected efficiency is greatly reduced by several loss mechanisms such as high bulk and surface recombination rates and slow kinetics for the oxygen evolution reaction. Combining Fe_2O_3 and WO_3 can improve the performance of the individual materials in several ways. Compared to bare WO_3, a larger spectral range is absorbed. The band alignment of Fe_2O_3 and WO_3 allows for the injection of electrons from Fe_2O_3 into WO_3, with the latter being a better electron conductor. Holes, on the other hand, are injected from WO_3 into Fe_2O_3 [17]. Sivula *et al* found the deposition of Fe_2O_3 onto WO_3 scaffolds to drastically improve electron charge collection [9]. Furthermore, the rate of the oxygen evolution reaction of Fe_2O_3 was shown to be significantly improved by surface treatment of Fe_2O_3 by a WO_3 layer [5, 18].

In addition to the strategies discussed above, nanostructuring is commonly employed to improve photoelectrodes [19, 20]. Several morphologies have so far been synthesized in the Fe_2O_3/WO_3 system, including flat and porous films [21–26], host-guest architectures [9], and nanowires [5, 10, 27]. Here, we for the first time systematically investigated the influence of the spatial distribution and the nanostructuring approach. WO_3 was applied both as a scaffold and as a surface treatment, allowing correlation between morphology and performance. Mesoporous Sn-doped Fe_2O_3 photoabsorber layers were prepared by a sol-gel approach and deposited onto a continuous, macroporous WO_3 scaffold [28]. We chose Sn-doped Fe_2O_3 following prior work in which we had shown that Sn increases the transfer efficiency and thereby the photocurrent. In the following, we are referring to Sn-doped Fe_2O_3 whenever we use the expression 'Fe_2O_3' to describe a sample or a component of one. The performance was increased even further by depositing a WO_3 surface layer and increasing the Fe_2O_3/WO_3 interfacial area, thus reaching photocurrents of up to 0.7 mA cm^{-2} at 1.23 V versus the reversible hydrogen electrode (RHE). The viability of this host-guest approach was confirmed by comparing the macroporous photoanodes to mesoporous reference samples [9, 10, 29–33]. As WO_3 only absorbs a small fraction of blue light, whereas hematite strongly absorbs in this region, measuring photocurrent transients under UV and under blue light illumination allowed for a more nuanced discussion of the impact of the morphology on the photoelectrochemical performance and gave further insights into a complex interplay of several effects such as transfer rate enhancement or increased light absorption.

2. Materials and methods

2.1. Preparation of WO_3 films

The precursor solution for WO_3 was prepared by adding 0.8 g of $(NH_4)_6H_2W_{12}O_{40} \cdot xH_2O$ to 3 ml of deionized water (Millipore Q). To create flat layers, this solution was dip-coated onto the fluorine doped tin oxide (FTO) substrate under ambient conditions at a rate of 38 mm min^{-1}. The samples were subsequently calcined at 500 °C with a ramp of 3 °C min^{-1} and a dwell time of 5 h. By applying the same procedure to polymethylmethacrylate (PMMA, synthesized according to a well-established procedure [29, 34, 35]) or hematite films, macroporous inverse opal scaffolds and overlayers, respectively, could be prepared.

2.2. Synthesis and deposition of tin-doped hematite

A procedure developed by Dunn *et al* [28] was applied for the synthesis of tin-doped hematite. 0.25 g Pluronic® P123 were dissolved in 10 ml *tert*-butanol under vigorous stirring. 0.1106 g (0.3 mmol) $Sn(CH_3COO)_4$ were added to the solution and stirred for 5 h. Next, $Fe(NO_3)_3 \cdot 9H_2O$ (0.505 g, 1.25 mmol) was added at room temperature and sonicated for 15 min. 2.5 ml water were then added and the solution was left to stir for 17 h under ambient conditions. Prior to spin coating, the resulting suspension was filtered through a filter with a pore diameter of 200 nm. The electrodes were prepared by depositing the filtered solution (100 μl) onto FTO or the macroporous scaffold, respectively, by spin coating at 1000 rpm for 30 s. The films were then calcined at 600 °C with a ramp of 3 °C min^{-1} and a dwell time of 30 min.

2.3. Crystallographic, structural and chemical analysis

Powder x-ray diffraction (XRD) patterns were acquired on a STOE powder diffractometer (Cu-Kα1, $\lambda = 1.5406$ Å) equipped with a position-sensitive Mythen-1K detector in transmission geometry.

Scanning electron microscopy (SEM) measurements were performed on a Zeiss Auriga scanning electron microscope with a field emission gun operated at 4 kV and equipped with an EDAX solid state energy-dispersive x-ray (EDX) spectroscopy detector.

Morphology, crystallography and elemental distribution were investigated using a probe-corrected FEI Titan Themis transmission electron microscope (TEM) with a high brightness field emission gun operating at 300 kV. Scanning TEM (STEM) images were acquired with an annular dark-field (ADF) detector and the distribution of Fe_2O_3 and WO_3 was mapped by collecting EDX spectra in STEM with four Super-X Bruker solid state detectors. Samples in cross-sectional geometry were prepared following a procedure developed by Strecker *et al* [36].

2.4. Optical characterization

UV–Vis spectra were measured under illumination through the substrate on a Perkin Elmer Lambda 1050 UV/Visible/NIR spectrophotometer with an integrating sphere. The absorbance of the films was calculated by measuring both transmittance and reflectance and correcting for the absorbance of the FTO substrate using an expression derived by Klahr *et al* [37].

2.5. Photoelectrochemical characterization

Current–voltage (CV) and incident photon-to-current efficiency (IPCE) curves were measured with a μ-Autolab III potentiostat with a FRA2 impedance analyzer. All but an area of 0.2 cm^2 was masked with a Teflon-coated glass fiber adhesive tape. The sample was placed into a quartz cell filled with an aqueous 0.1 M NaOH electrolyte and connected, with an Ag/AgCl reference electrode and a Pt mesh counter electrode, to the potentiostat. To obtain CV curves, the films were illuminated through the substrate by an AM 1.5 solar simulator (Solar Light Model 16S) at 100 mW cm^{-2} by scanning from negative to positive potentials in the dark or under illumination at a sweep rate of 20 mV s^{-1}.

IPCE measurements were performed under monochromatic light chopped with a frequency of 1 Hz. Samples were illuminated through the substrate by a 150 W Xenon lamp equipped with a monochromator and order-sorting filters. All IPCE values were measured at a sample bias of 1.23 V versus RHE under simulated solar irradiation. The light intensity at the electrode was determined using a certified, KG5-filtered Fraunhofer ISE silicon reference cell.

Photocurrent transient data were acquired with a 365 nm or a 455 nm light-emitting diode and a chopping frequency of 2 Hz at an applied potential of 1.23 V versus RHE. The light intensities were calibrated with a Fraunhofer ISE silicon certified photovoltaic cell and correspond to 3.2 mA (160 W m^{-2}). Transfer efficiencies were calculated as the ratio of the steady-state and the initial photocurrent density. As transfer efficiencies measured with 365 nm light did not deviate by more than $\pm$2% from those measured with 455 nm light and are effectively independent of the illumination wavelength, the transfer efficiencies averaged over both wavelengths will be discussed.

3. Results and discussion

Two series of samples were prepared by sol-gel synthesis (figure 1).

The first series of flat layers served as references to the host-guest electrodes and allowed analyzing performance-enhancing factors on simple model systems. This series comprised three samples, including a compact WO_3 and a mesoporous Fe_2O_3:Sn layer coated onto FTO as well as a dual absorber photoelectrode prepared by depositing a WO_3 overlayer onto a Fe_2O_3:Sn film. These samples are labeled 'WO_3', 'Fe_2O_3' and 'Fe_2O_3/WO_3', respectively. The second series demonstrated the performance-enhancing benefits of the host-guest architecture. A macroporous WO_3 scaffold was infiltrated by Fe_2O_3:Sn and coated with an additional WO_3 overlayer. In the remainder of the text, these samples are labeled 'mWO_3', 'mWO_3/Fe_2O_3', and '$mWO_3/Fe_2O_3/WO_3$', respectively. It should be noted that WO_3 is known to potentially fulfill several functions. At wavelengths below the optical absorption limit, WO_3 acts as a photoabsorber. Due to its favorable band alignment, it can also act as a majority charge carrier collector of electrons generated in Fe_2O_3 [9]. Finally, WO_3 can act as a surface treatment to Fe_2O_3 photoanodes, suppressing electron–hole recombination on the surface [5]. The samples in this study were prepared so that all three possible performance-enhancing effects could be studied systematically.

XRD patterns confirmed the successful synthesis of phase-pure Fe_2O_3:Sn in the hematite structure and of monoclinic WO_3 (figure SI 1) (stacks.iop.org/MRX/4/016409/mmedia) [38, 39]. Other phases or reaction products could not be detected by XRD, SEM or TEM. In accordance with previous work by Dunn *et al*, cross-sectional analysis of mesoporous Fe_2O_3 layers showed ~50 nm thick mesoporous films composed of individual nanoparticles with an average size of ~40 nm $\times$ 80 nm (figures 2(b) and (c)) [28]. WO_3, in contrast, forms ~100 nm thick, cracked layers composed of large, compact platelets between a few hundred nanometers and a few micrometers in size (figure SI 2). The Fe_2O_3/WO_3 dual absorber retains these morphologies, with WO_3 both infiltrating the Fe_2O_3 layer, with an accumulation at the FTO, and forming a ~50 nm thick layer on top (figures 2(a), (c) and (d)). By forming a compact top layer, WO_3 decreases the exposed Fe_2O_3 surface area.

In contrast, the macroporous samples have an open, porous morphology (figure 2(d)). The macroporous WO_3 scaffold forms a ~2.5 μm thick layer with ~150 nm wide pores (figure 2(g)). Even though the scaffold is distorted compared to a perfect inverse opal structure, it is continuous and reaches the back contact. This should

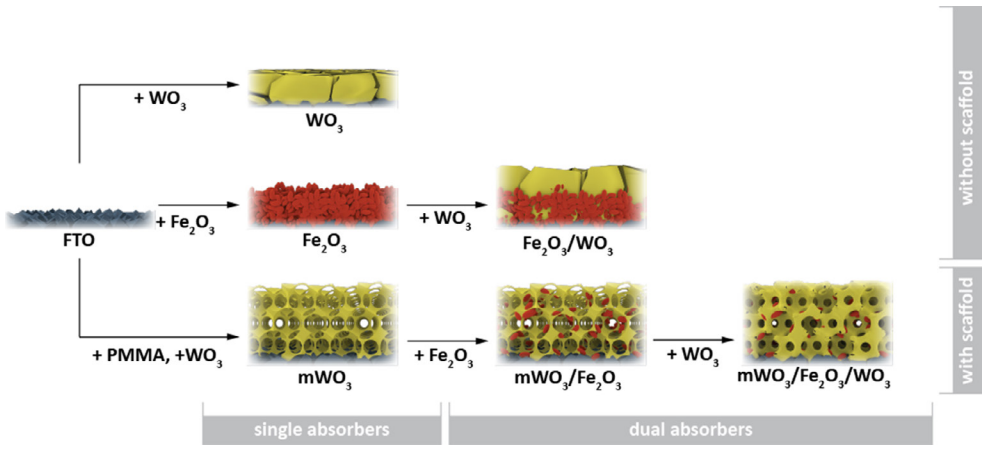

Figure 1. Schematic showing the synthesis procedures of all samples.

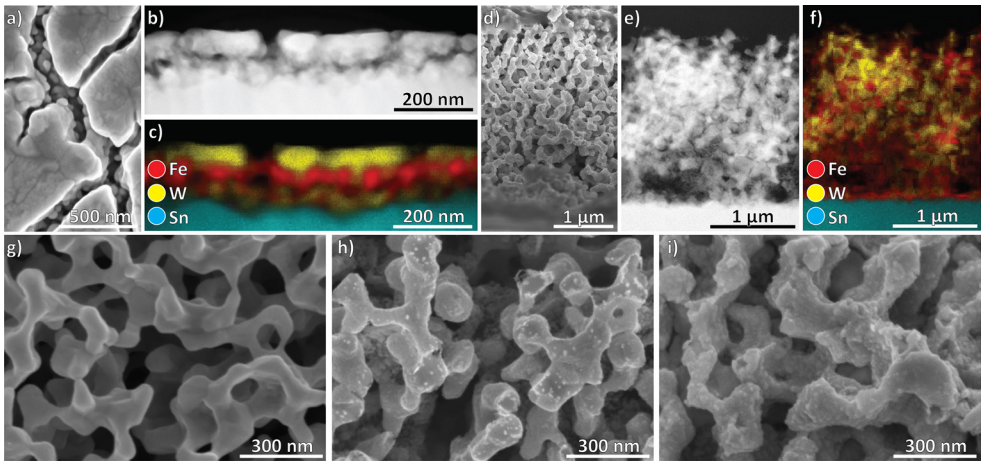

Figure 2. Morphological characterization. (a) Top-view SEM image of the Fe_2O_3/WO_3 thin films. Fe_2O_3 is visible through cracks in the WO_3 layer. ADF-STEM images and EDX maps of Fe_2O_3/WO_3 are shown in (b) and (c). (d) Cross-section SEM image of $mWO_3/Fe_2O_3/WO_3$. ADF-STEM images and EDX maps of $mWO_3/Fe_2O_3/WO_3$ are shown in (e) and (f). Compared to the pure WO_3 scaffold shown in (g), deposited Fe_2O_3 nanoparticles are clearly seen in (h). In (i) a SEM image of $mWO_3/Fe_2O_3/WO_3$ is shown. By depositing a WO_3 overlayer, the whole structure is coated.

be beneficial for charge transport. Hematite nanoparticles fully infiltrate the scaffold and are homogenously distributed throughout the whole film (figures 2(e) and (f)). An additional thin layer of Fe_2O_3 nanoparticles forms on the FTO substrate (figure 2(f)). In contrast to the flat layers, a WO_3 overlayer fully infiltrates the scaffold and thinly coats WO_3 scaffold and Fe_2O_3 nanoparticles alike without top layer formation (figure 2(i)).

The crystal structures of the materials were investigated by TEM. Monocrystallinity of hematite nanoparticles prepared by this synthesis procedure has previously been shown by Dunn *et al* [28]. Both the WO_3 scaffold and the WO_3 overlayer are highly crystalline, with mWO_3 having domains of several hundred nanometers in size (figures 3(a) and (b)). In both Fe_2O_3/WO_3 and mWO_3/Fe_2O_3, an abrupt interface between Fe_2O_3 and WO_3 without specific orientation relationships or amorphous phases was found (figure 3(c)).

Light absorption of all samples was assessed with UV–Vis measurements (figure 4). Like the photoelectrochemical measurements, they were done under substrate illumination.

As expected from the band gap, bare WO_3 only absorbs light up to a wavelength of ~425 nm. In comparison, Fe_2O_3 absorbs light up to a wavelength of ~560 nm, consistent with a band gap of 2.2 eV, and thereby a much larger percentage of the solar spectrum. Of the flat layers, Fe_2O_3 absorbs more light than WO_3 throughout the whole spectral range. In both flat and macroporous samples, more light is absorbed upon deposition of a mesoporous Fe_2O_3:Sn layer or a WO_3 overlayer. Notable is the strong scattering contribution of both compact and macroporous WO_3, which is reduced for all *dual* absorbers (figures 4(c) and (f)). As the UV–Vis spectra were acquired under substrate illumination, light must be backscattered by WO_3 and absorbed by the Fe_2O_3 layer. WO_3 acting as a reflective layer in the visible range (figures 4(c) and (f)) significantly increases the absorbance (figure 4(b) and (e)). Unfortunately, this increase in absorbance is not expected to contribute to the photocurrent, as it is above the absorption cut-off of both Fe_2O_3 and WO_3. However, future studies, in which an additional photoabsorber is introduced, might benefit from this increase in scattering.

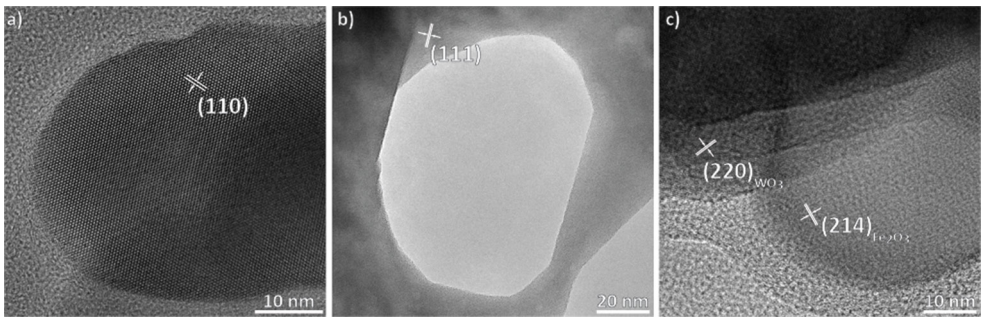

Figure 3. HRTEM images of (a) the WO_3 overlayer in Fe_2O_3/WO_3 and (b) the WO_3 scaffold. (c) Interface between Fe_2O_3 and WO_3.

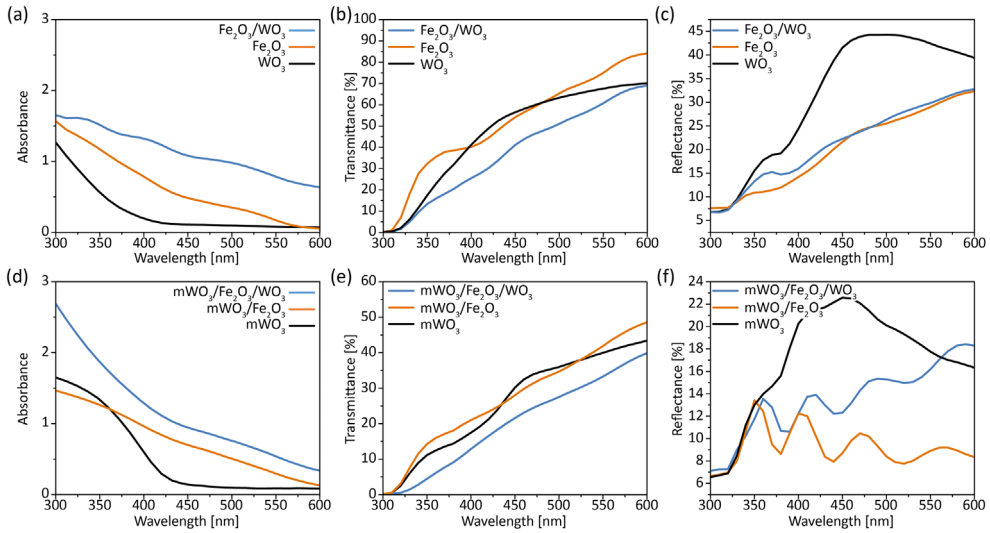

Figure 4. UV–Vis, transmittance and reflectance spectra of mesoporous ((a)–(c)) and macroporous ((d)–(f)) samples.

All samples were photoelectrochemically characterized by CV measurements under AM 1.5 illumination and by IPCE measurements (figure 5). Among the flat layers, Fe_2O_3 has a higher current density than WO_3 (0.01 mA cm^{-2} at 1.23 V versus RHE compared to 0.08 mA cm^{-2} at 1.23 V versus RHE), which can be explained by increased light harvesting in the visible region. In accordance with the drop in light absorbance seen in the UV–Vis spectra, the IPCE spectrum of bare WO_3 drops to 0% at ~425 nm, whereas the IPCE spectrum of Fe_2O_3 drops to 0% at a much longer wavelength of ~560 nm. Depositing a WO_3 layer onto Fe_2O_3, thus creating a dual absorber, increases the current density threefold compared to Fe_2O_3 and 17-fold compared to WO_3, with currents of 0.23 mA cm^{-2} at 1.23 V versus RHE and a maximum IPCE of up to 13% at 340 nm. This dual absorber not only outperforms the single components, but also the sum of current densities obtained from the individual absorber layers, suggesting that the increased performance cannot be explained solely by increased light absorption. Another important feature of the dual absorber photoanodes is a cathodic shift of the onset potential by nearly 200 mV. Such a shift is usually attributed to the reduction of loss pathways due to either charge transfer catalysis or suppression of surface recombination [40–42].

The macroporous films show trends similar to the flat layer model systems (figure 5). The performance of the macroporous WO_3 scaffolds (0.13 mA cm^{-2} at 1.23 V versus RHE) is strongly increased compared to WO_3 flat layers. As shown by UV/Vis measurements, the deposition of Fe_2O_3 leads to increased light absorption in the visible range and a shift of the IPCE curve, increasing the current density up to 0.24 mA cm^{-2} at 1.23 V versus RHE. A substantial performance increase to 0.7 mA cm^{-2} at 1.23 V versus RHE with a maximum IPCE of 17% at 350 nm is achieved by depositing an additional WO_3 layer. As for Fe_2O_3/WO_3, CV measurements of $mWO_3/Fe_2O_3/WO_3$ show a steep current onset at 0.8 V versus RHE. mWO_3/Fe_2O_3, which is also composed of both materials, does not show such a steep onset. The strong performance increases compared to flat layers could be explained by the increase in porosity and therefore surface area, or by the WO_3 scaffold acting as a current collector as described in the literature [9, 29]. Of note is the strong performance rise when applying WO_3 as a surface layer compared to having it as a scaffold. Interface-related effects such as suppressed recombination due to the WO_3 surface layer could therefore play a major role. Another possible explanation is the role of WO_3 as a scattering layer, which would increase the light harvesting efficiency of Fe_2O_3.

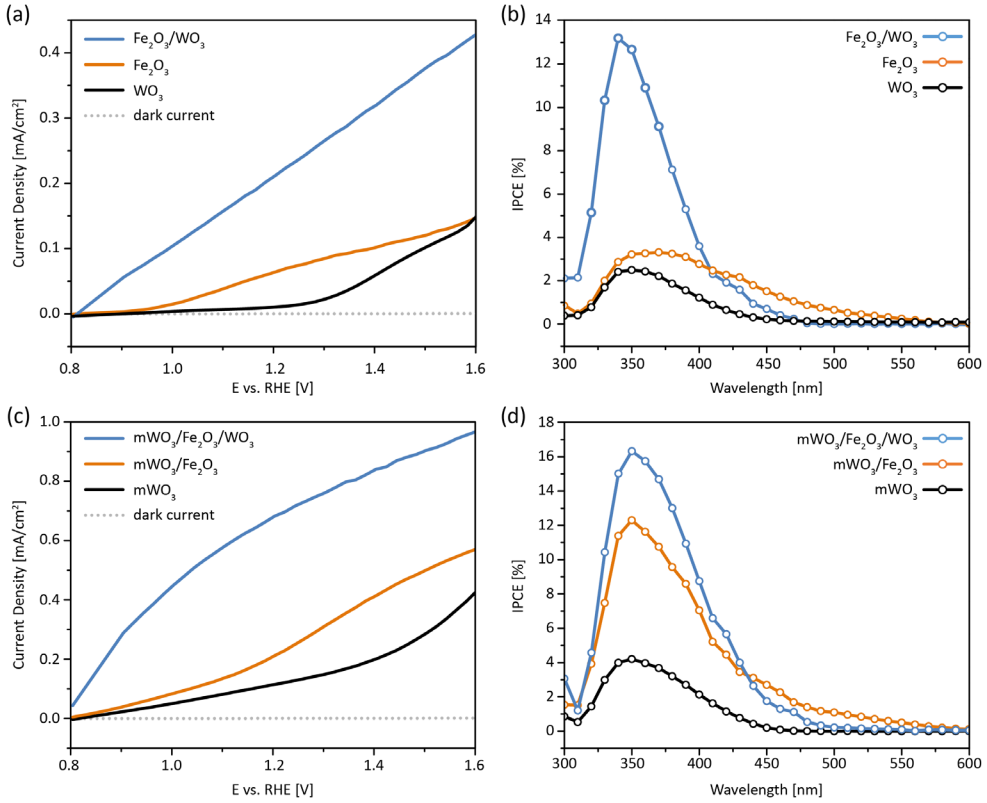

Figure 5. CV and IPCE measurements of flat ((a) and (b)) and macroporous layers ((c) and (d)) measured under AM 1.5 illumination. As the dark currents of all samples overlapped, only one measurement is shown.

The photocurrents discussed so far were measured under AM 1.5 illumination. However, given the band structures of Fe_2O_3 and WO_3 and based on our UV/Vis measurements, different processes are expected to take place under illumination with UV and with visible light (figure SI 3) [17]. Under UV illumination, electrons generated in Fe_2O_3 can be injected into WO_3 and holes generated in WO_3 can be injected into Fe_2O_3 (figure 6(a)), with the WO_3 scaffold expected to reduce recombination by efficient charge transport to the FTO substrate. Light of a longer wavelength, however, only generates electron–hole pairs in Fe_2O_3, of which the electrons can, according to the band diagram, be injected into WO_3 (figure SI 3). To gain further insight into the behavior of the dual absorber system, photocurrent transients were measured under chopped illumination with UV (365 nm) and blue (455 nm) light. Due to increased light absorption by both Fe_2O_3 and WO_3 in the UV region, steady-state photocurrents acquired under UV illumination are consistently higher than those measured with blue light (figure 6(b)). WO_3 is a highly efficient photocatalyst, leading to higher photocurrents than Fe_2O_3 under UV illumination [15]. Blue light, however, is not absorbed by WO_3 (figure 4) and Fe_2O_3 reaches higher photocurrents.

Photocurrent transients reflect all processes influencing charge transfer and transport in the electrode (figure 6) [28, 43]. Upon illumination, movement of photo-generated holes to the surface leads to a charging or displacement current. If holes accumulate, either due to slow surface kinetics or due to slow electron transport to the back contact, they recombine with electrons, and the initial photocurrent decays to a lower steady-state photocurrent. For Fe_2O_3, this leads to a characteristic 'spike and overshoot' photocurrent, whereas fast surface kinetics and good electron conductivity of pure WO_3 lead to a rectangular transient form suggestive of complete charge carrier extraction [43]. By depositing Fe_2O_3 onto a WO_3 scaffold, the difference between initial and steady-state photocurrent decreases compared to Fe_2O_3 and deposition of an additional WO_3 layer brings the shape of the photocurrent transient even closer to a rectangle. As expected from the fast surface kinetics and good charge transport properties the material is known for, both WO_3 and mWO_3 have transfer efficiencies of 100% [15]. In comparison and in accordance with previous work by Dunn *et al*, Sn-doped Fe_2O_3 has a transfer efficiency of 41% [28]. The transfer efficiency can be improved to 75% by depositing the Sn-doped Fe_2O_3 layer onto a WO_3 scaffold. In line with discussion in the literature, the WO_3 scaffold could act as a charge collector and thereby increase the electron diffusion length [9, 29]. In comparison, surface treatment by the deposition of an additional WO_3 layer has a greater effect on the transfer efficiency than the introduction of a WO_3 scaffold and increases the transfer efficiency to 85 and 88% for flat Fe_2O_3/WO_3 and macroporous $mWO_3/Fe_2O_3/WO_3$, respectively. The improved performance might stem from an enhanced rate of Faradaic reactions on the interface due to the surface treatment with WO_3. For both illumination wavelengths, photocurrent densities reached by the dual absorbers, regardless of whether WO_3

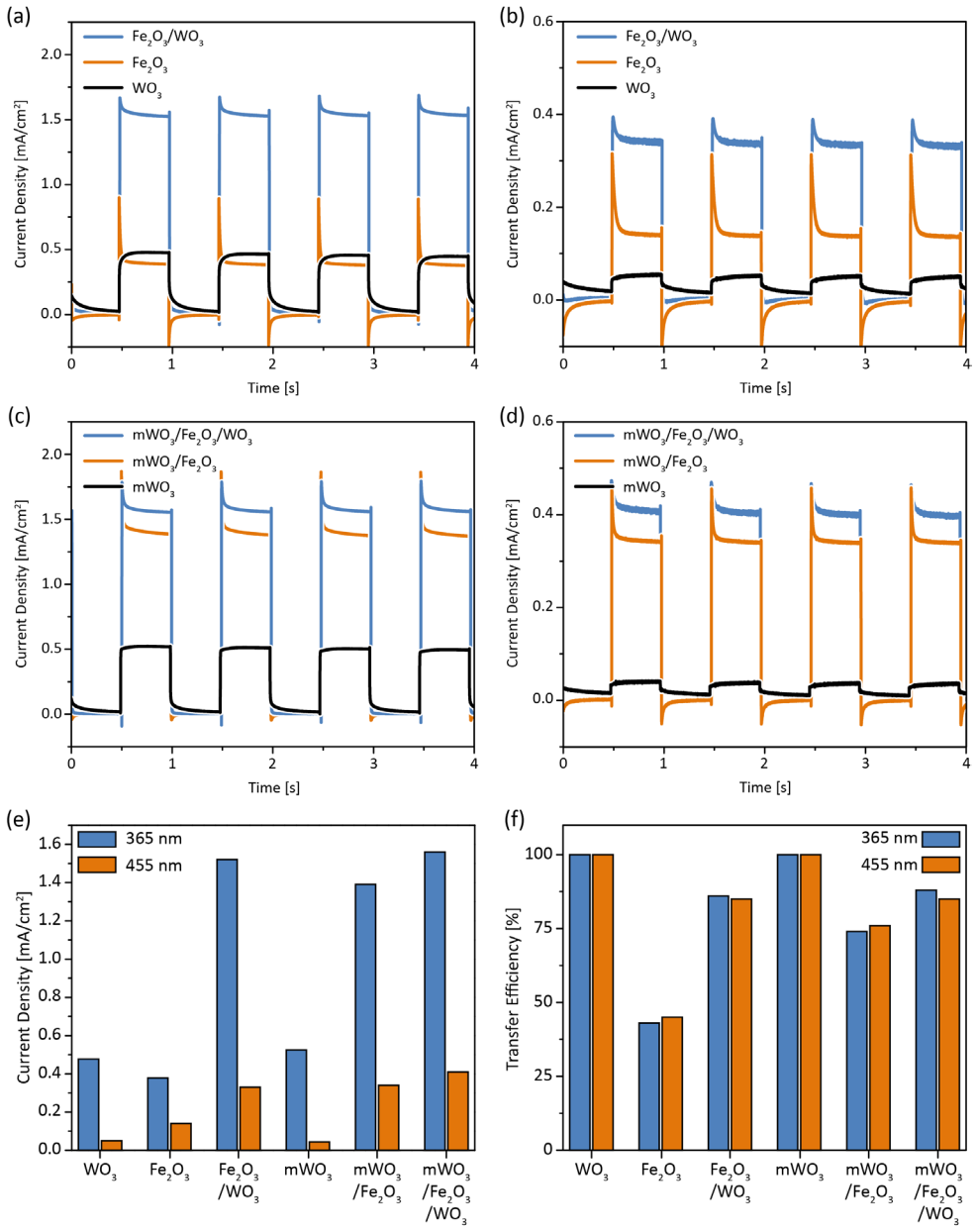

Figure 6. Photocurrent transients of flat layers under (a) UV (365 nm) and (b) blue (455 nm) illumination at an applied potential of 1.23 V versus RHE. Photocurrent transients of the macroporous layers under 365 nm and 455 nm illumination are shown in (c) and (d), respectively. (e) Steady-state photocurrent densities under illumination with 365 nm and 455 nm light at a potential of 1.23 V versus RHE. (f) Transfer efficiencies under illumination with 365 nm and 455 nm light extracted from photocurrent transients measured at 1.23 V ca. RHE.

was applied as a surface layer or as a scaffold, are very similar. This is in contrast to measurements under the full AM 1.5 solar spectrum, where a much larger difference in photocurrent densities was observed for the different architectures. This can presumably be explained by a complex interplay of several factors, such as faster surface kinetics, improved current collection and enhanced light absorption, in which WO_3 beneficially influences Fe_2O_3.

4. Conclusions

To systematically analyze the effects of WO_3 on Fe_2O_3 for photoelectrochemical water splitting, dual absorbers were prepared with WO_3 as a scaffold and/or as a surface layer. Both approaches significantly increased the performance, validating both the host-guest and the surface layer approach. By combining them, current densities of 0.7 mA cm^{-2} at 1.23 V versus RHE under AM 1.5 illumination with an IPCE of 17% at 350 nm were reached. The performance increase was investigated by CV, IPCE, photocurrent transient and UV–Vis measurements and we could identify several beneficial effects responsible for improved charge carrier generation and transport. WO_3 strongly reflects visible light which in the dual absorbers is then absorbed by Fe_2O_3, resulting in increased light harvesting and thus higher photocurrents. Compared to Fe_2O_3, a cathodic shift of the onset potential from 1.0 to

0.8 V and an increase in transfer efficiencies, reaching up to 88%, were measured. We conclude that the investigated device architecture is a promising approach for the design of Fe_2O_3/WO_3 dual absorber photoanodes by combining different beneficial effects of different materials to produce substantially improved devices.

Acknowledgments

The work was supported by the German Research Foundation (DFG) via the priority program SPP 1613, the Nanosystems Initiative Munich (NIM) and LMUexcellent, the Bavarian research network 'Solar Technologies Go Hybrid', and the Center for Nanoscience (CeNS). We thank the students Zachary Edelen and Marina Polo Collado for participating in the research. Steffen Schmidt and Halina Dunn are gratefully acknowledged for insightful discussions.

References

[1] Fujishima A and Honda K 1972 Electrochemical photolysis of water at a semiconductor electrode *Nature* **238** 37–8
[2] Grätzel M 2001 Photoelectrochemical cells *Nature* **414** 338–44
[3] Hisatomi T, Kubota J and Domen K 2014 Recent advances in semiconductors for photocatalytic and photoelectrochemical water splitting *Chem. Soc. Rev.* **43** 7520–35
[4] Li Z, Luo W, Zhang M, Feng J and Zou Z 2013 Photoelectrochemical cells for solar hydrogen production: current state of promising photoelectrodes, methods to improve their properties, and outlook *Energy Environ. Sci.* **6** 347–70
[5] Kronawitter C X, Vayssieres L, Shen S, Guo L, Wheeler D A, Zhang J Z, Antoun B R and Mao S S 2011 A perspective on solar-driven water splitting with all-oxide hetero-nanostructures *Energy Environ. Sci.* **4** 3889
[6] Wang J, Han Y, Feng M, Chen J, Li X and Zhang S 2011 Preparation and photoelectrochemical characterization of WO_3/TiO_2 nanotube array electrode *J. Mater. Sci.* **46** 416–21
[7] Su J, Guo L, Bao N and Grimes C A 2011 Nanostructured $WO_3/BiVO_4$ heterojunction films for efficient photoelectrochemical water splitting *Nano Lett.* **11** 1928–33
[8] Luan P, Xie M, Liu D, Fu X and Jing L 2014 Effective charge separation in the rutile TiO_2 nanorod-coupled α-Fe_2O_3 with exceptionally high visible activities *Sci. Rep.* **4** 6180–6
[9] Sivula K, Formal F Le and Grätzel M 2009 WO_3–Fe_2O_3 photoanodes for water splitting: a host scaffold, guest absorber approach *Chem. Mater.* **21** 2862–7
[10] Jin T, Diao P, Wu Q, Xu D, Hu D, Xie Y and Zhang M 2014 WO_3 nanoneedles/a-Fe_2O_3/cobalt phosphate composite photoanode for efficient photoelectrochemical water splitting *Appl. Catal.* B **148–9** 304–10
[11] Sivula K, Le Formal F and Grätzel M 2011 Solar water splitting: progress using hematite (α-Fe_2O_3) photoelectrodes *ChemSusChem* **4** 432–49
[12] Hodes G, Cahen D and Manassen J 1976 Tungsten trioxide as a photoanode for a photoelectrochemical cell (PEC) *Nature* **260** 312–3
[13] Liu X, Wang F and Wang Q 2012 Nanostructure-based WO_3 photoanodes for photoelectrochemical water splitting *Phys. Chem. Chem. Phys.* **14** 7894
[14] Granqvist C G 2000 Electrochromic tungsten oxide films: review of progress 1993–1998 *Sol. Energy Mater. Sol. Cells* **60** 201–62
[15] Santato C, Ulmann M and Augustyński J 2001 Photoelectrochemical properties of nanostructured tungsten trioxide films *J. Phys. Chem.* B **105** 936–40
[16] Murphy A B, Barnes P R F, Randeniya L K, Plumb I C, Grey I E, Horne M D and Glasscock J A 2006 Efficiency of solar water splitting using semiconductor electrodes *Int. J. Hydrog. Energy* **31** 1999–2017
[17] van de Krol R, Liang Y and Schoonman J 2008 Solar hydrogen production with nanostructured metal oxides *J. Mater. Chem.* **18** 2311
[18] Kishi T and Aritsuka M 1988 Photo-anodic behaviour of α-ferric oxide film electrodes coated with various metal oxides *Surf. Coat. Technol.* **34** 345–53
[19] Osterloh F E 2013 Inorganic nanostructures for photoelectrochemical and photocatalytic water splitting *Chem. Soc. Rev.* **42** 2294–320
[20] Zhang P, Gao L, Song X and Sun J 2015 Micro- and nanostructures of photoelectrodes for solar-driven water splitting *Adv. Mater.* **27** 562–8
[21] Luo W, Yu T, Wang Y, Li Z, Ye J and Zou Z 2007 Enhanced photocurrent–voltage characteristics of WO_3/Fe_2O_3 nano-electrodes *J. Phys. D: Appl. Phys.* **40** 1091–6
[22] Memar A, Daud W R W, Hosseini S, Eftekhari E and Minggu L J 2010 Study on photocurrent of bilayers photoanodes using different combination of WO_3 and Fe_2O_3 *Sol. Energy* **84** 1538–44
[23] Hosseini S, Eftekhari E, Masoudi Soltani S, Memar A, Eghbali Babadi F, Dastorian Jamnani B, Ismail M H S and Jeffery Minggu L 2013 Effect of intermediate layer in photocurrent improvement of three-layer photoanodes using WO_3 and Fe_2O_3 *J. Environ. Chem. Eng.* **1** 1309–14
[24] Hosseini S, Eftekhari E, Masoudi Soltani S, Babadi F E, Minggu L J and Ismail M H S 2014 Synthesis, characterization and performance evaluation of three-layered photoanodes by introducing a blend of WO_3 and Fe_2O_3 for dye degradation *Appl. Surf. Sci.* **289** 53–61
[25] Mao A, Kim J K, Shin K, Wang D H, Yoo P J, Han G Y and Park J H 2012 Hematite modified tungsten trioxide nanoparticle photoanode for solar water oxidation *J. Power Sources* **210** 32–7
[26] Miecznikowski K, Ramírez A, Fiechter S, Bogdanoff P, Szaniawska E, Wadas A and Kulesza P J 2015 Development of hybrid tungsten oxide photoanodes admixed with borododecatungstate-polyanion modified-hematite: enhancement of water oxidation upon irradiation with visible light *Electrochim. Acta* **179** 379–85
[27] Li Y, Feng J, Li H, Wei X and Wang R 2016 Photoelectrochemical splitting of natural seawater with a-Fe_2O_3/WO_3 nanorod arrays *Int. J. Hydrog. Energy* **41** 4096–105
[28] Dunn H K, Feckl J M, Müller A, Fattakhova-Rohlfing D, Morehead S G, Roos J, Peter L M P, Scheu C and Bein T 2014 Tin doping speeds up hole transfer during light-driven water oxidation at hematite photoanodes *Phys. Chem. Chem. Phys.* **16** 24610–20
[29] Kondofersky I, Dunn H K, Müller A, Mandlmeier B, Feckl J M, Fattakhova-Rohlfing D, Scheu C, Peter L M and Bein T 2015 Electron collection in host-guest nanostructured hematite photoanodes for water splitting: the influence of scaffold doping density *ACS Appl. Mater. Interfaces* **7** 4623–30

[30] Riha S C, Devries Vermeer M J, Pellin M J, Hupp J T and Martinson A B F 2013 Hematite-based photo-oxidation of water using transparent distributed current collectors *ACS Appl. Mater. Interfaces* **5** 360–7
[31] Sun Y, Chemelewski W D, Berglund S P, Li C, He H, Shi G and Mullins C B 2014 Antimony-doped tin oxide nanorods as a transparent conducting electrode for enhancing photoelectrochemical oxidation of water by hematite *ACS Appl. Mater. Interfaces* **6** 5494–9
[32] Wang L, Palacios-Padrós A, Kirchgeorg R, Tighineanu A and Schmuki P 2014 Enhanced photoelectrochemical water splitting efficiency of a hematite-ordered Sb:SnO_2 host-guest system *ChemSusChem* **7** 421–4
[33] Tsui K, Zhang Y, Yang S and Fan Z 2014 Efficient photoelectrochemical water splitting with ultrathin films of hematite on three-dimensional nanophotonic structures *Nano Lett.* **14** 2123–9
[34] Mandlmeier B, Minar N K, Feckl J M, Fattakhova-Rohlfing D and Bein T 2014 Tuning the crystallinity parameters in macroporous titania films *J. Mater. Chem.* A **2** 6504
[35] Liu Y, Peters K, Mandlmeier B, Müller A, Fominykh K, Rathousky J, Scheu C and Fattakhova-Rohlfing D 2014 Macroporous indium tin oxide electrode layers as conducting substrates for immobilization of bulky electroactive guests *Electrochim. Acta* **140** 108–15
[36] Strecker A, Salzberger U and Mayer J 1993 Specimen preparation for transmission electron microscopy: reliable method for cross-sections and brittle materials *Prakt. Metallogr.* **30** 482–95
[37] Klahr B M, Martinson A B F and Hamann T W 2011 Photoelectrochemical investigation of ultrathin film iron oxide solar cells prepared by atomic layer deposition *Langmuir* **27** 461–8
[38] Maslen E N, Streltsov V A, Streltsova N R and Ishizawa N 1994 Synchrotron x-ray study of the electron density in a-Fe_2O_3 *Acta Crystallogr.* B **50** 435–41
[39] Tanisaki S 1960 Crystal structure of monoclinic tungsten trioxide at room temperature *J. Phys. Soc. Japan* **15** 573–81
[40] Hisatomi T, Le Formal F, Cornuz M, Brillet J, Tétreault N, Sivula K and Grätzel M 2011 Cathodic shift in onset potential of solar oxygen evolution on hematite by 13-group oxide overlayers *Energy Environ. Sci.* **4** 2512
[41] Tilley S D, Cornuz M, Sivula K and Grätzel M 2010 Light-induced water splitting with hematite : improved nanostructure and iridium oxide catalysis *Angew. Chem., Int. Ed. Engl.* **122** 6549–52
[42] Zhong D K, Sun J, Inumaru H and Gamelin D R 2009 Solar water oxidation by composite catalyst/r-Fe_2O_3 photoanodes *J. Am. Chem. Soc.* **131** 6086–7
[43] Peter L M, Wijayantha K G U and Tahir A A 2012 Kinetics of light-driven oxygen evolution at α-Fe_2O_3 electrodes *Faraday Discuss.* **155** 309–22